ENSO Phase Transitions in a Warming Climate: A Multi-Model Large Ensemble Analysis

Brandon A. Molina[1], Sara C. Sanchez[1], Clara Deser[2], Nicola Maher[3,4], and Pedro DiNezio[1,5]

[1]Department of Atmospheric and Oceanic Sciences, University of Colorado, Boulder, CO, USA
[2]National Center for Atmospheric Research, Boulder, CO, USA
[3]Research School of Earth Sciences, Australian National University, Canberra, Australia
[4]ARC Centre of Excellence for 21st Century Weather, Australia
[5]ATLAS Institute, University of Colorado, Boulder, CO, USA

Key Points:

- Greenhouse warming shifts maximum tropical Pacific air sea coupling eastward in eight of ten models
- Coupling shifts are associated with thermocline shoaling and increased El Niño frequency across models
- Eastward shifts are linked to more La Niña to El Niño transitions especially after multi-year events but responses vary across models

Corresponding author: B. A. Molina, brandon.molina@colorado.edu

Abstract

Transitions between ENSO phases are asymmetric in the modern climate: while El Niño reliably gives way to La Niña conditions, La Niña events more often persist or return to a neutral state than transition into El Niño conditions. This one-sided transition preference represents a fundamental breakdown of a fully oscillatory ENSO cycle. It is unclear if this asymmetric oscillatory behavior will change as the climate warms due to increasing greenhouse gas (GHG) concentrations. Using 10 different model Large Ensembles under a range of GHG forcing scenarios, we show that warming systematically alters the spatial structure of tropical Pacific air-sea coupling during boreal spring. Most models project an eastward shift of the region of maximum air-sea coupling as a forced response to GHG increases. In addition, all models show enhanced oscillatory ENSO behavior, which manifests as more frequent El Niño events and a higher probability of La Niña-to-El Niño event transitions, particularly for multi-year La Niña events. These findings illustrate that the longitude of maximum air-sea coupling has a structural control on projected changes in ENSO through its effect on the efficiency of thermocline feedbacks.

Plain Language Summary

In the tropical Pacific, the El Niño-Southern Oscillation (ENSO) swings between warm (El Niño) and cool (La Niña) phases, affecting weather worldwide. However, ENSO does not swing evenly: El Niño events reliably transition into La Niña, while La Niña events often persist for multiple years without transitioning into El Niño. This asymmetry prevents ENSO from behaving like a balanced oscillation. In this work, we use output from 10 climate models running multiple simulations under high greenhouse gas emission pathways to investigate whether this uneven behavior changes as the planet warms. Our central result is that in most models, the region where the ocean and atmosphere interact most strongly shifts toward the eastern Pacific under greenhouse warming. This shift positions ocean-atmosphere interactions over a region where subsurface ocean temperatures more effectively influence surface conditions. As this coupling region shifts eastward, ENSO becomes more balanced: El Niño events become more frequent, and La Niña events are more likely to transition into El Niño, particularly after multi-year events. These findings suggest that greenhouse warming may alter the rhythm of ENSO, with impli-

cations for rapid swings between contrasting weather in regions such as the western United States, Australia, and Southeast Asia.

1 Introduction

The El Niño-Southern Oscillation (ENSO) phenomenon is characterized by quasi-periodic fluctuations between warm (El Niño) and cold (La Niña) sea-surface temperature (SST) anomalies in the equatorial Pacific, with recurrence times ranging from 2-7 years (McPhaden et al., 2006; Trenberth, 1997). However, ENSO does not operate as a symmetric oscillator: El Niño-to-La Niña transitions are substantially more common than La Niña-to-El Niño transitions, contributing to the rarity of sustained El Niño conditions (Kessler, 2002; Okumura & Deser, 2010; Jia et al., 2025). This asymmetry reflects distinct termination mechanisms: rapid heat discharge after El Niño leads to the onset of La Niña conditions, whereas slow heat recharge allows La Niña to persist across consecutive years (DiNezio & Deser, 2014). While considerable attention has been directed toward projected changes in ENSO amplitude, spatial pattern, and event frequency under greenhouse warming (Cai et al., 2015, 2018), the mechanisms that control when and how the system flips from one state to another, remain understudied. This gap limits our ability to predict the duration and termination of events, to anticipate cascading teleconnected impacts on global climate, and to assess whether the present-day asymmetries between ENSO phases will persist or be reshaped in a warming climate.

At a fundamental level, ENSO's oscillatory behavior is governed by the interplay between the Bjerknes feedback (Bjerknes, 1969), which provides the reinforcing coupling necessary for phase maintenance, and the recharge-oscillator mechanism, which controls the timing of termination (Jin, 1997). Transitions to the opposite state are triggered only after the equatorial warm water volume has been sufficiently recharged or discharged to act as delayed negative feedback (Meinen & McPhaden, 2000). Because the Bjerknes feedback is inherently asymmetric—typically stronger during El Niño than La Niña due to the nonlinear dependence of atmospheric deep convection on SST (Graham & Barnett, 1987; Kang & Kug, 2002)—changes in the mean state may disproportionately affect one transition pathway over the other, potentially reshaping the historical imbalance between rapid El Niño terminations and prolonged multi-year La Niña events (DiNezio & Deser, 2014). In the modern climate, this feedback is strongest in the central Pacific within the Niño-3.4 domain—where SST anomalies most efficiently engage the atmospheric wind

response and vice versa. Equilibrium simulations spanning glacial to greenhouse conditions have revealed that this air-sea coupling maximum shifts zonally with the mean state, moving westward during glacial periods and eastward under extreme warming (Molina et al., 2026), altering the efficiency of thermocline feedbacks and the oscillatory behavior of ENSO. In the modern climate, the central Pacific location of maximum air-sea coupling limits the thermocline feedback. In the central Pacific, where the thermocline is deeper than in the eastern Pacific, temperature anomalies within the thermocline generated during a La Niña event have limited ability to influence SST through vertical thermal advection. These anomalies sit well below the mixed layer, limiting the ability of La Niña to trigger subsequent El Niño events. In contrast, in the eastern Pacific, where the mean thermocline is shallow, subsurface temperature anomalies generated during La Niña events strongly influence SST through vertical thermal advection, enabling regular transitions back to El Niño. Thus, ENSO's oscillatory behavior is heavily influenced by the longitude of maximum air-sea coupling and not only the strength of the air-sea coupling. Under greenhouse warming, the coupling region shifts eastward as the equatorial Pacific mean state warms, repositioning the Bjerknes feedback and altering its sensitivity to perturbations (Molina et al., 2026). This raises the hypothesis that changes in coupling longitude may contribute to documented shifts in ENSO behavior under warming, including increased multi-year La Niñas (Geng et al., 2023), more frequent transitions from multi-year La Niña to strong El Niño (Jia et al., 2025), and more extreme El Niño events (Cai et al., 2014). However, the relationship between coupling longitude and ENSO transition likelihood has not been systematically quantified across multiple models.

Detecting shifts in the statistics of ENSO phase transitions is inherently challenging due to their relatively infrequent occurrence (Conti et al., 2017; Freund et al., 2024) and the pronounced internal variability that modulates ENSO on decadal and multidecadal timescales (Wittenberg, 2009; Deser et al., 2012). Large ensemble simulations provide a rigorous framework for overcoming this signal-to-noise challenge by generating a multitude of realizations under identical radiative forcing (Deser et al., 2020). By comparing multiple model large ensembles, it is possible to evaluate model structural uncertainty in both the characteristics of internal variability and forced change (Maher et al., 2023). While single-model evidence has established the coupling-shift mechanism in equilibrium simulations (Molina et al., 2026), a systematic multi-model large ensemble evaluation

of ENSO's oscillatory behavior and its dependence on the location of air-sea coupling under transient forcing has yet to be attempted.

Here, we evaluate the evolution of ENSO's oscillatory behavior within a transient warming climate using RCP8.5, SSP585 and SSP370 scenarios in ten model large ensembles from the Multi Model Large Ensemble Archive version 2 (MMLEAv2; (Maher et al., 2025)).

2 Data and Methods

2.1 Multi-Model Ensemble and Observational Data

We use ten model large ensembles from the Coupled Model Intercomparison Project (CMIP), archived in the Multi-Model Large Ensemble Archive version 2 (MMLEAv2) and remapped to a common 2.5°x2.5° grid (Maher et al., 2025). We select all models in the MMLEAv2 that provide both monthly sea surface temperature (SST) and zonal wind stress (τ_x) fields and contain at least 18 ensemble members, ensuring sufficient sampling of internal variability. This results in four CMIP5 models (CanESM2 (Kirchmeier-Young et al., 2017), CESM1 (Kay et al., 2015), MPI-GE (Maher et al., 2019), and GFDL-CM3 (Sun et al., 2018)) and six CMIP6 models (CanESM5 (Swart et al., 2019), CESM2 (Rodgers et al., 2021), MPI-GE-CMIP6 (Olonscheck et al., 2023), ACCESS-ESM1-5 (Ziehn et al., 2020), E3SMv2 (Fasullo et al., 2024), and MIROC6 (Tatebe et al., 2019)) (See Table 1). The CMIP5 models are forced with historical radiative forcing up to 2005 and Representative Concentration Pathway 8.5 (RCP8.5) thereafter. The CMIP6 models follow historical forcing from 1950 to 2014 and then from 2015 to 2100 either the Shared Socioeconomic Pathway 5-8.5 (SSP5-8.5) [CanESM5, MPI-GE-CMIP6, ACCESS-ESM1-5 and MIROC6] or SSP3-7.0 [CESM2 and E3SMv2]. Of the models run with multiple emission scenarios, we select the high-emission RCP8.5 and SSP5-8.5 scenarios to maximize the signal-to-noise ratio of the forced response, enabling statistically robust detection of shifts in transition statistics that might be obscured under lower-emission pathways.

We analyze model output over the period 1950–2100. The 1950 start date is chosen to coincide with the beginning of the reliable instrumental record and to provide a 50-year historical baseline (1950–1999) for comparison with the late twenty-first century (2050–2099). To isolate internal variability, we compute anomalies for each ensemble mem-

ber by subtracting the ensemble mean at each time step and grid point. This approach simultaneously removes the forced trend and the seasonal cycle, yielding anomalies that represent internally generated variability only (Deser et al., 2012; Maher et al., 2019). Because the ensemble mean is computed at each time step rather than over a fixed reference period, this method accounts for the non-stationary nature of the forced response, including seasonally varying patterns of greenhouse gas-induced warming.

We compare simulations with observations using two independent SST products: the Extended Reconstructed Sea Surface Temperature version 5 (ERSSTv5; (Huang et al., 2017)) and the Hadley center Sea Ice and SST dataset version 1.1 (HadISST v1.1; (Rayner et al., 2003)), both provided as part of the MMLEAv2 on a 2.5°x2.5° grid for the period 1950-2024. For observed zonal wind stress, we use the European center for Medium-Range Weather Forecasts (ECMWF) Ocean Reanalysis System 5 (ORAS5; (Zuo et al., 2019)), available for the period 1958-2018, which we linearly interpolate from its native 1° resolution to the common 2.5°x2.5° grid for consistency with the MMLEAv2. Monthly anomalies for each observational dataset are computed by removing the 1981-2010 climatology—the conventional reference period in most observational ENSO studies—and quadratically detrending over the full available record of each dataset independently, approximating the removal of the forced response in the single observational realization.

2.2 Definition of ENSO Events and Phase Transitions

ENSO events are defined using a modified Niño3.4 (N3.4-m) index following (Molina et al., 2026). Rather than using the fixed Niño3.4 region (5°S–5°N, 170°W-120°W), SST anomalies are averaged over a model-specific region (5°S–5°N) centered on the longitude of maximum SST anomaly variability in DJF during 1950–1999 to best capture each model's unique representation of ENSO variability (Table 1; Figure S1 in Supporting Information S1). The model-specific longitudinal bounds are defined by the longitudes at which averaged equatorial SST variability is 93% of its peak—a threshold that, in observations, recovers a region approximately 50° wide, consistent with the Niño3.4 domain. This calibration yields narrower regions in most models, with peak variability located closer to the eastern Pacific Niño3 region (e.g., CanESM5, ACCESS, E3SMv2, GFDL-CM3, MIROC6), while others have peak variability in the central Pacific closer to the Niño4 region (e.g., CESM2, MPI-GE, MPI-GE-CMIP6) (Table 1; Figure S1 in Supporting Information S1).

While this modified region does not substantially alter the total number of identified events compared to using the conventional Niño3.4 region, it ensures that the N3.4-m index captures each model's actual center of SST variability, minimizing biases introduced by the fixed standard box in models with displaced cold tongues or shifted variability peaks. DJF is chosen because it captures the peak of the ENSO cycle, when anomalies are most fully developed and the phase of the event is most clearly expressed (Trenberth, 1997). An El Niño event is identified when the DJF N3.4-m index exceeds +0.5 standard deviations (s.d.), a La Niña event when it falls below -0.5 s.d., and neutral conditions otherwise. The ±0.5 s.d. threshold normalizes for inter-model differences in ENSO amplitude and is consistent with recent multi-model assessments of ENSO statistics under greenhouse warming (Geng et al., 2023; Jia et al., 2025). The s.d. is computed separately for each ensemble member over the 1950–1999 reference period to account for sampling uncertainty in ENSO amplitude while maintaining a consistent baseline across the archive. The root-mean-square s.d. across ensemble members for each model is listed in Table 1. For observations, the 1981-2010 reference period and ±0.5 s.d. thresholds are applied to each SST product independently.

La Niña events are further classified by duration. A multi-year La Niña is identified when La Niña conditions persist for two or more consecutive DJF seasons; otherwise, the event is classified as a single-year La Niña. For the transition analysis, multi-year La Niña events are represented by their terminal year—the final consecutive DJF season meeting the La Niña threshold—so that transitions from multi-year La Niña capture the phase the system evolves into after a prolonged cold event. All La Niña events are also analyzed as a single combined category; the single-year and multi-year distinction is applied as an additional decomposition to examine whether La Niña persistence influences subsequent transition behavior. We compute the frequency of occurrence of each phase (or phase frequency) by counting the total number of DJF seasons classified as El Niño, La Niña, or Neutral within each 50-year window, expressed as events per 50 years. Changes in frequency are evaluated by comparing the 1950–1999 historical baseline to the 2050–2099 period, allowing direct quantification of how the occupancy of each ENSO state shifts under sustained greenhouse forcing.

We quantify ENSO phase transitions by counting the reversals in active ENSO phases between consecutive DJF seasons. For each year, the phase in DJF of the initial year is compared to the phase in DJF of the following year. To track temporal evolution, tran-

Table 1. Summary of Large Ensemble Models used in this study from MMLEAv2.

Model	**Members**	**Forcing**	**N3.4-m bounds**	**S.D. (°C)**	ΔSST_{TP} **(°C)**
CMIP5					
CanESM2	50	RCP8.5	150–110°W	1.18	2.97
CESM1	40	RCP8.5	170–120°W	1.30	2.57
GFDL-CM3	20	RCP8.5	135–110°W	1.27	3.37
MPI-GE	100	RCP8.5	170°E–165°W	0.90	1.98
CMIP6					
ACCESS-ESM1-5	40	SSP5-8.5	125–105°W	0.72	2.94
CanESM5	18	SSP5-8.5	130–105°W	0.79	3.84
CESM2	100	SSP3-7.0	170–135°W	1.62	2.59
E3SM-v2	21	SSP3-7.0	135–105°W	1.20	2.30
MIROC6	50	SSP5-8.5	150–115°W	1.41	2.05
MPI-CMIP6	30	SSP5-8.5	175°E–160°W	1.02	2.06

Note. N3.4-m represents the modified Niño3.4 index, S.D. represents the root-mean-square of the N3.4-m standard deviation (S.D.) across ensemble members over the period 1950–1999. ΔSST_{TP} represents the ensemble mean SST change over the Tropical Pacific (TP) region (20°S–20°N, 120°E–80°W) between 1950–2000 and 2050–2100.

sition probabilities—defined as the fraction of events in a given initial phase that evolve into El Niño, La Niña, or neutral conditions in the following year—are computed in rolling 50-year windows advancing by 1 year across the 1950–2100 period. We compute the probability of transitions independently for each ensemble member and then average the probabilities across members to obtain the ensemble-mean transition probability. For observational reference, phase transition statistics are computed over the 1950–1999 period and compared against the spread of individual ensemble members over the same historical window to assess whether observed transition behavior falls within the range of simulated transition behavior.

2.3 Air-Sea Coupling Analysis

To characterize the dominant mode of air-sea coupling during the ENSO transition season (Mar-Apr-May; MAM), we perform Maximum Covariance Analysis (MCA; (Bretherton et al., 1992)) between SST and zonal wind stress (τ_x) anomalies averaged over this season across the tropical Pacific (15°S-15°N, 120°E-80°W). MAM is chosen because it coincides with the boreal spring persistence barrier (Webster & Yang, 1992; Torrence & Webster, 1998), the season when ENSO events are most likely to either decay to neutral or flip to the opposite phase (Stuecker et al., 2013). During this window, the Bjerknes feedback reaches its seasonal minimum, leaving the coupled system highly vulnerable to perturbations that determine whether the existing phase persists or transitions. The MCA is computed independently for each ensemble member. A sign convention is enforced such that positive SST anomalies in the central equatorial Pacific correspond to the positive phase of the MCA mode. For observations, the MCA is computed over the overlapping period (1958-2018) of the SST and τ_x records. We focus our analysis on the leading MCA mode. We use the heterogeneous SST regression map, obtained by regressing SST anomalies onto the standardized τ_x expansion coefficient, to identify the spatial structure of air-sea coupling associated with the MCA mode. We quantify this spatial structure by identifying the longitude of the maximum value in the mean 5°S–5°N profile of the SST heterogeneous regression pattern. Shifts in this peak longitude indicate a reorganization of the location where Pacific SST anomalies most efficiently engage the atmospheric wind response. Additionally, we consider the Squared Covariance Fraction (SCF)—the fraction of total squared covariance between SST and τ_x explained by the leading mode—to measure the overall strength of the air-sea coupling across the analysis domain. Higher SCF values indicate that the leading mode captures a larger fraction of the coupled variability.

The MCA analysis is repeated in rolling 50-year windows advancing by 1 year, consistent with the transition probability analysis, to track the co-evolution of coupling structure and ENSO transition behavior across the entire 1950–2100 period. The change in peak longitude between the historical (1950–1999) and late 21st century (2050–2099) periods quantifies the magnitude and direction of zonal shift for each model.

2.4 Statistical Significance

We assess the statistical significance of projected changes using two complementary approaches. The uncertainty of the ensemble-mean change is represented by the 95% confidence interval, estimated from the inter-member spread using a two-tailed Student's t-distribution. However, within each model, differences in the frequency of ENSO phases, phase transition probabilities, and coupling metrics between the historical (1950–1999) and late 21st century (2050–2099) periods are evaluated using a two-tailed Welch's t-test at the 95% confidence level ($p < 0.05$). Welch's t-test is employed rather than Student's t-test because it does not assume equal variances between the two periods, accommodating potential changes in ensemble-member spread under transient forcing.

3 Results

3.1 Present-day ENSO characteristics

The monthly lead-lag autocorrelation function (ACF) of the N3.4-m index provides a fundamental diagnostic of ENSO persistence and oscillatory behavior, representing the rate of signal decay and the tendency for phase reversal at specific temporal lags (Figure 1a). There is a wide range of behavior in the ACF across models, particularly at a 12-month lag (Figures 1a and 1b). This disagreement reflects that the combined ACF conflates the divergent dynamics of El Niño and La Niña, which are governed by distinct feedback pathways (Takahashi & Dewitte, 2016). Indeed, the phase-specific ACF (e.g., by considering only El Niño samples and only La Niña samples) shows greater agreement between models and observations (Figures 1c–f). By distinguishing between warm and cold ENSO states, the ten-model ensemble converges more closely upon the observed asymmetry in ENSO transition dynamics: a rapid, discharge-driven termination of El Niño events and a persistence of La Niña (Figures 1c–f). Specifically, 9 out of 10 models replicate the rapid El Niño transition to La Niña conditions while 5 out of 10 models replicate the prolonged La Niña decay at the 12-month interval, aligning with observational benchmarks from ERSSTv5 and HadISST. This improved agreement shows that while the aggregate ACF appears noisy, the phase-specific ACF more clearly discriminates the governing physical mechanisms—namely the rapid discharge of equatorial heat content during El Niño and the slower recharge process sustaining La Niña—that are more consistently captured across the large-ensembles, validating their ability to represent the cou-

pled oceanic-atmospheric feedbacks that dictate year-to-year ENSO predictability and transition regularity.

We further diagnose the realism of the tropical Pacific air-sea coupling across the multi-model large ensembles with MCA analysis between SST and τ_x anomalies during MAM (Figure 2). During MAM, the climatological zonal SST gradient and trade winds across the tropical Pacific are weakest, allowing small-scale perturbations to dictate whether an anomaly will persist, grow, or transition into the opposite phase. The ensemble-mean heterogeneous regression maps (Figure 2a) highlight the model diversity in the meridional extent of the coupled SST and τ_x patterns. The meridional SST structure relative to observations (Figure 2b) shows that models differ in the longitudinal position of their coupling maximum, while the longitudinal center of action for each ensemble member (Figure 2c) reveals substantial spread within and across models. However, despite these structural differences, the high SCF in all models (72.5%–94.2%) confirms that the leading MCA mode consistently dominates the boreal spring air-sea interactions.

We focus on the equatorial profile of this oceanic response by taking the meridional average (5°S–5°N) of the SST heterogeneous patterns (Figure 2b), to highlight the varying magnitude and spatial expression of this air-sea coupling region associated with each model. Relative to observational benchmarks—ERSSTv5 and HadISST (peaking near 150°W and 160°W respectively)—the models exhibit systematic biases in their longitudinal "center of action" (Figure 2c). Quantifying the center of action for individual ensemble members reveals distinct regimes of spatial bias and intra-ensemble variance (Figure 2c). Models such as ACCESS and GFDL-CM3 exhibit a pronounced eastward bias relative to observations, characterized by a tight agreement across their ensembles. Although CESM2 and CanESM5 similarly display an eastward bias in their center of action, they display a broad longitudinal spread among members, indicating higher internal variability in the spatial anchoring of the feedback (Figure 2c). In stark contrast, MPI-GE maintains a westward bias and narrow range of variability, highlighting that the structural positioning of the spring Bjerknes feedback remains a primary source of inter-model divergence. These historical differences in spatial anchoring could moderate the efficiency of the recharge/discharge processes governing ENSO transition regularity, providing a critical baseline for testing the sensitivity of transition dynamics to projected 21st-century warming.

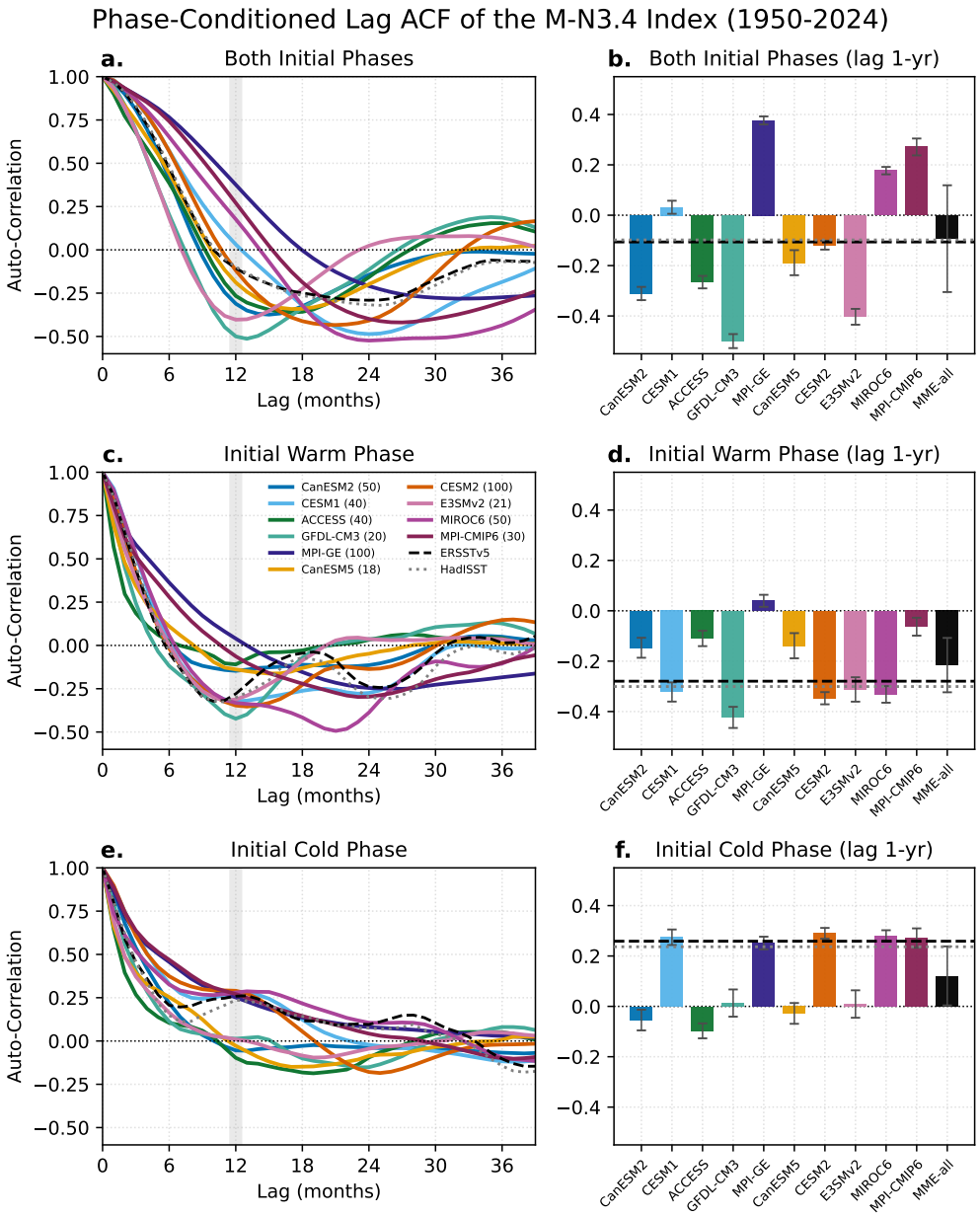

Figure 1. (a), (c), and (e) Autocorrelation function (ACF) for the N3.4-m index in ten model large ensembles compared to observational benchmarks of the Niño3.4 index from ERSSTv5 (dashed black) and HadISST (dotted grey). (c) tracks events initialized in El Niño conditions (positive anomaly exceeding +0.5 standard deviations (s.d.)), and (e) tracks events initialized in La Niña conditions (negative anomaly below –0.5 s.d.). (b), (d), and (f) Bar charts showing the ACF at a 1-year lag corresponding to (a), (c), and (e), respectively. Vertical grey shading in (a), (c), and (e) highlights the 12-month lag to specifically quantify year-to-year predictability and transition regularity. Error bars represent the 95% confidence interval of the ensemble-mean ACF (two-tailed Student's t-test).

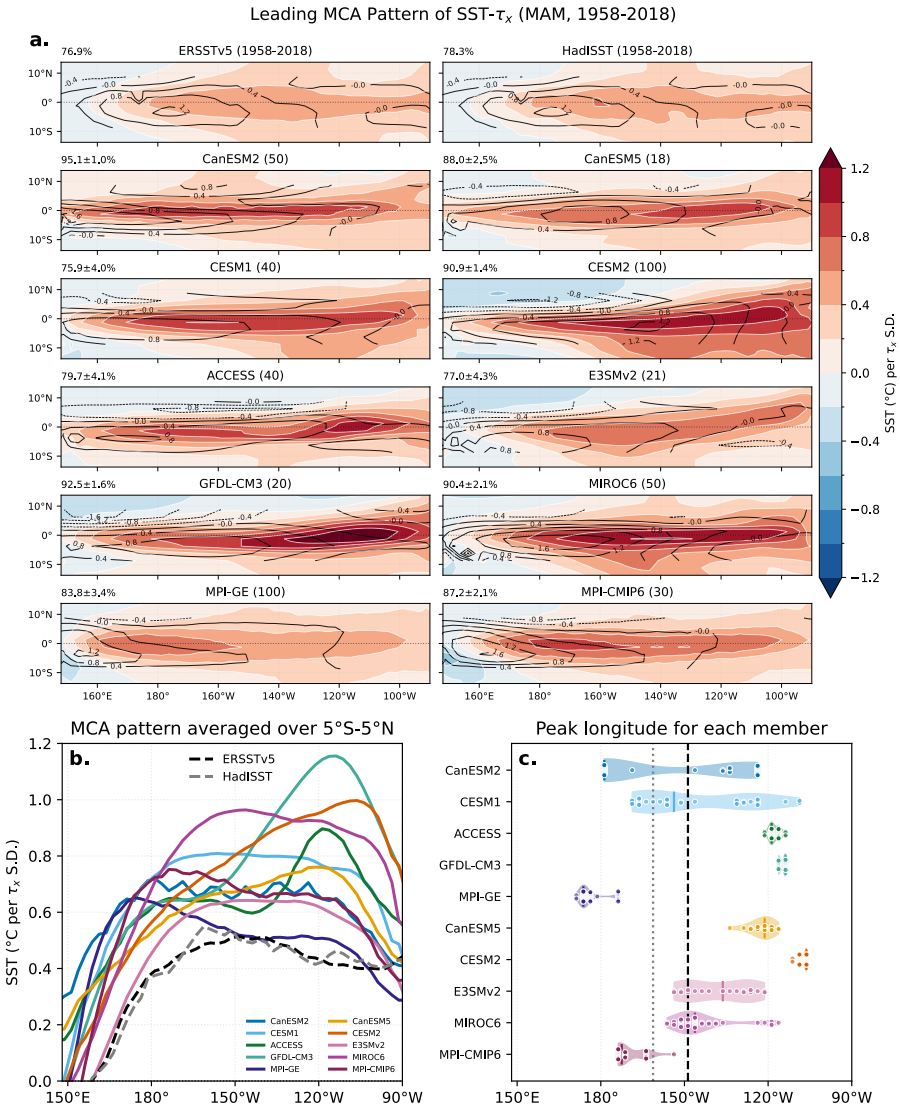

Figure 2. (a) The ensemble means spatial heterogeneous regression maps for the leading Maximum Covariance Analysis (MCA) mode during (Mar-Apr-May) MAM (1958-2018). Shaded patterns denote SST anomalies (°C per τ_x S.D.) and contours denote τ_x anomalies ($10^{-2}N/m^2$ per SST S.D.). For each map, the ensemble size is indicated in parentheses next to the model's name, and the squared covariance fraction (SCF) of the leading mode (inter-ensemble spread) is provided in the top-left corner. (b) The meridional average (5°S–5°N) of the SST heterogeneous patterns in (a) compared to the observational benchmarks (ERSSTv5; black dashed and HadISST; grey dashed lines). (c) The longitudinal "center of action" for each ensemble member of each model, where dots represent individual members and the distribution is shown via violin plots. Vertical dashed and dotted lines indicate the peak longitudes for ERSSTv5 and HadISST, respectively.

3.2 Future changes in air-sea coupling region

Under transient 21st-century radiative forcing, the longitude and strength of the MAM air-sea coupling maximum change in the majority of models, though the sign and magnitude of the response vary across models. The spatio-temporal evolution of these changes is illustrated via time-longitude sections of equatorial SST anomalies for each model (Figure 3a, Figure S2 in Supporting Information S1). Tracking this evolution with a 50-year sliding window reveals an eastward drift in the peak longitude of the leading MCA mode in 8 of the 10 models, emerging prominently after the 1990–2040 window (Figure 3b). By 2050–2099, all 10 models exhibit statistically significant zonal shifts relative to the 1950–1999 historical baseline ($p < 0.05$, two-tailed Welch's t-test; Figure 3c). Among these, eight models shift eastward—with three (CESM1, CESM2, and E3SMv2) exceeding 20° of displacement—while two models (ACCESS and CanESM5) exhibit substantial westward shifts exceeding 15°. Due to this inter-model divergence in sign, the multi-model ensemble mean shift is not statistically distinguishable from zero at the 95% confidence level.

Concurrently, the leading MCA mode intensifies under warming across all models (Figure S3a in Supporting Information S1). By the late 21st century (2050–2099), every model projects an increase in SCF relative to the historical baseline (Figure S3b in Supporting Information S1), with particularly pronounced strengthening in E3SMv2 (ΔSCF $\approx +9\%$) and ACCESS (ΔSCF $\approx +7\%$). However, these forced changes in coupling strength bear no meaningful relationship to the zonal shifts of the coupling center (Figure S4 in Supporting Information S1), indicating that the intensification and the spatial displacement of the air-sea coupling region are driven by distinct aspects of the evolving mean state (Figure S4 in Supporting Information S1).

The eastward shift of the air-sea coupling maximum likely occurs as part of a broader tropical Pacific mean-state reorganization under greenhouse warming. Models that simulate a weakening of the west–east equatorial SST gradient under increasing radiative forcing generally exhibit larger eastward shifts in the longitude of maximum air-sea coupling (Figure S5 in Supporting Information S1). This is consistent with the projected eastward shift of atmospheric convection under greenhouse warming (Vecchi & Soden, 2007; Cai et al., 2014, 2015), which would reposition the region of strongest air-sea interaction. The magnitude of the forced shift relative to sampling fluctuations associated

with finite record length and number of ensemble members, however, differs substantially across models. We consider a signal-to-noise ratio (SNR) defined as the ensemble-mean longitude shift divided by the standard deviation of coupling longitude across ensemble members. By this measure, CESM2 (SNR = 4.15), E3SMv2 (1.56), GFDL-CM3 (1.45), CESM1 (1.34), and CanESM5 (1.17), exhibit strong forced signals, with the ensemble-mean eastward displacement exceeding the historical spread. ACCESS (0.97) also shows detectable forced shifts, though with greater overlap with sampling uncertainty. By contrast, CanESM2 (0.49), MPI-GE-CMIP6 (0.43), MIROC6 (0.41), and MPI-GE-CMIP5 (0.21) have historical spreads much larger than the forced shift, implying that sampling uncertainty strongly modulates the longitude of maximum coupling in those models. While the detectability of the shift in air-sea coupling is model dependent, the consistent forced shift underscores that the air-sea coupling region is not fixed and responds systematically to background climate warming. This behavior is consistent with Molina et al. (2026), who showed that the longitude of maximum air-sea coupling varies with the mean state from glacial to greenhouse forcing in a single model (CESM1).

The forced eastward shift of the maximum air-sea coupling center found in most models alters the key physical feedbacks that govern ENSO phase evolution, in particular processes related to ocean dynamics. Under present-day climate conditions, the spring air-sea coupling center is anchored over the central Pacific, positioning it over a deep climatological thermocline. In this spatial configuration, surface wind anomalies cannot easily tap into the subsurface ocean; consequently, phase evolution relies heavily on weaker thermodynamic processes like the SST-evaporation feedback, making the La Niña-to-El Niño transition notoriously inefficient because residual warm anomalies fail to amplify (DiNezio & Deser, 2014; Molina et al., 2026). However, as greenhouse warming drives the coupling center eastward, the atmospheric center of action is displaced directly over the shallow climatological thermocline of the eastern Pacific cold tongue. This spatial reorganization triggers a regime shift in ENSO dynamics: wind stress anomalies can now efficiently modulate the shallow thermocline, allowing subsurface temperature anomalies to immediately alter SSTs through powerful vertical advection (the thermocline feedback). While the opposite El Niño-to-La Niña transition is already efficiently driven by rapid, basin-wide equatorial heat discharge and remains less sensitive to spatial shifts, the warming-induced eastward displacement specifically unlocks the thermocline feedback for La Niña termination.

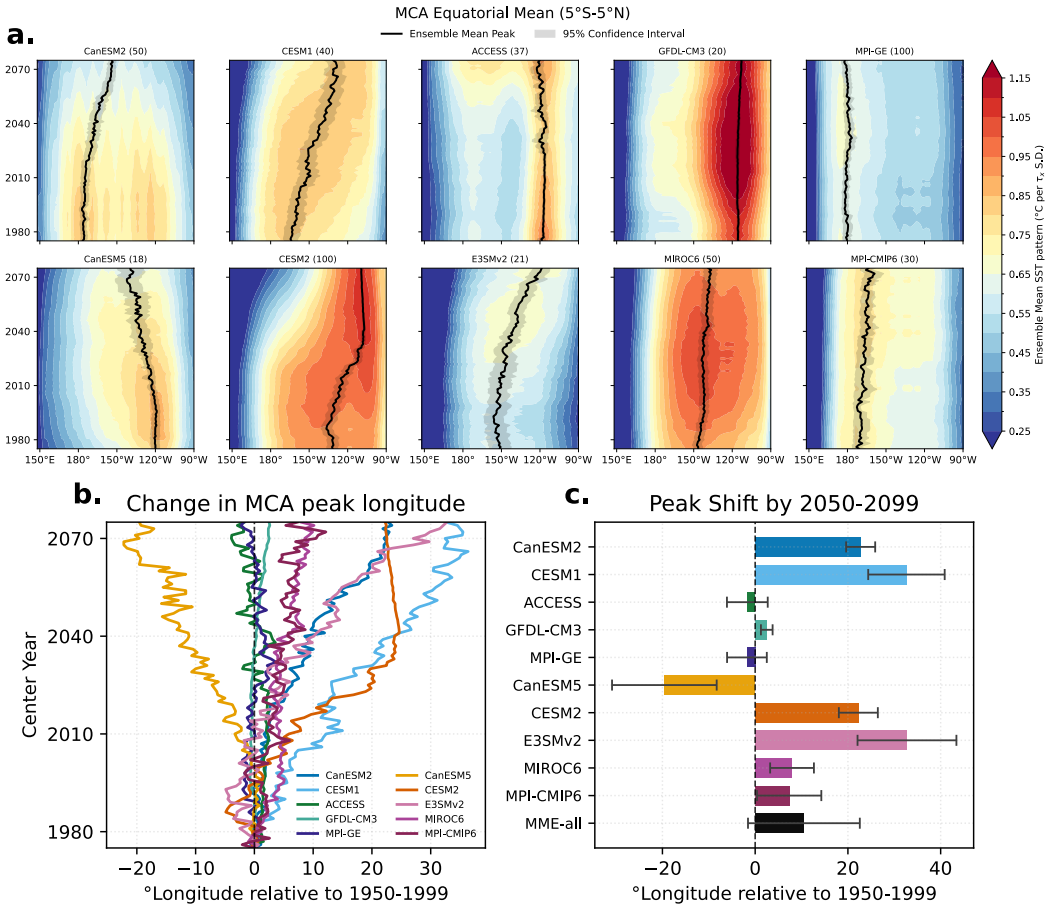

Figure 3. (a) Hovmöller-style diagrams illustrating the evolution of the meridional mean (5°S–5°N) SST heterogeneous patterns (°C per τ_x S.D.) for each model. The y-axis represents the center year of a 50-year sliding window, and the solid black curve denotes the ensemble mean of the peak longitudes identified independently for each ensemble member and each 50-year running window. For each member, the peak longitude is determined after averaging the SST pattern over 5°S–5°N. (b) The temporal trajectory of the zonal shift in the peak air-sea coupling longitude relative to the historical baseline (1950–1999). (c) Projected shift in peak longitude by the 2050–2099 period relative to the historical baseline, with positive values denoting an eastward shift. Error bars represent the 95% confidence interval of the ensemble-mean change (two-tailed Student's t-test).

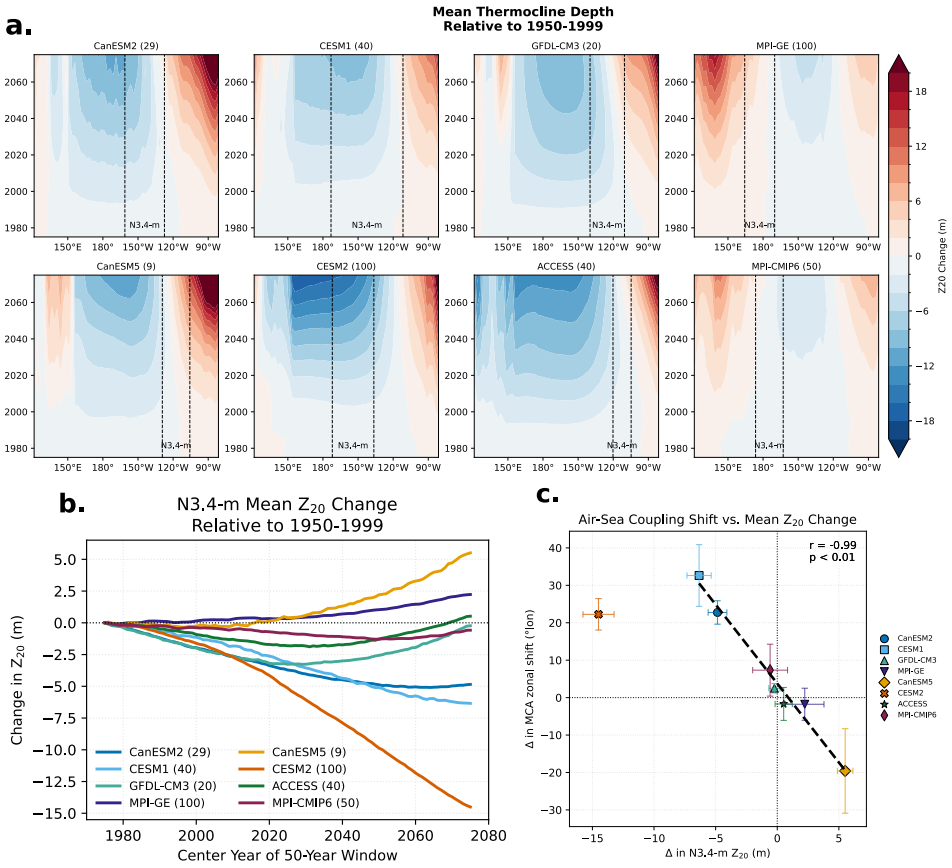

Figure 4. (a) Contour plots showing the longitudinal-temporal evolution of equatorial-averaged (5°S–5°N) Z_{20} change (depth of the 20°C isotherm, in meters; relative to the 1950–1999 historical baseline) for each large ensemble model. The x-axis denotes longitude across the Pacific, and the y-axis shows the center year of each 50-year running window. Shading indicates the ensemble mean Z_{20} change (blue for shoaling, red for deepening), with the number of ensemble members for each model indicated in parentheses. The region between the dashed vertical lines indicates the model's modified Niño 3.4 (N3.4-m) window. (b) Temporal evolution of thermocline depth anomalies: 50-year running window anomalies of the N3.4-m Z_{20} relative to the historical baseline (1950–1999). Curves represent the ensemble mean for each large ensemble model. (c) Inter-model relationship: Scatter plot illustrating the relationship between the change in the N3.4-m Z_{20} (x-axis) and the zonal shift of the air-sea coupling region (y-axis; in degrees longitude) by 2050–2099. Negative zonal values indicate a westward shift, while positive values represent an eastward shift. Colored markers represent the ensemble mean of each model, with horizontal and vertical error bars denoting the 95% confidence interval of the respective change for each model. The solid black line indicates the linear regression fit across the multi-model ensemble.

This mechanistic link is supported by the relationship between the forced change in thermocline depth and the zonal shift of the coupling region across the multi-model ensemble. We use the depth of the 20°C isotherm (Z_{20}) to approximate the depth of the thermocline in the tropical Pacific, a widely used proxy in ENSO studies (Kessler, 1990; Fedorov & Philander, 2001; Li & Xie, 2014; Li et al., 2015, 2016; Geng et al., 2019). Among the selected models in the MMLEAv2, 8 provide an available Z_{20} field, enabling this analysis. We acknowledge that Z_{20} is an imperfect approximation of the true thermocline depth, as it may not fully capture regions where the thermocline is diffuse or exhibits multiple layers (Yang & Wang, 2009). Furthermore, background warming can change the depth of the 20°C isotherm independently of changes in thermocline structure, meaning that Z_{20} shoaling or deepening may reflect both genuine thermocline adjustments and uniform warming of the water column. Nevertheless, Z_{20} provides a consistent and physically meaningful metric for comparing thermocline depth changes across models. Among the 8 models with an available Z_{20} field, the magnitude of thermocline shoaling within the N3.4-m region is strongly correlated with the eastward displacement of the coupling maximum ($r = -0.85$, not shown). This relationship strengthens considerably when excluding CESM2 ($r = -0.99$, $p < 0.01$; Figure 4c), which appears as an outlier in the regression. CESM2 exhibits the largest thermocline shoaling by the late 21st century (∼15 m), yet its coupling region shifts only ∼20° eastward. This anomalous behavior arises because CESM2's coupling region is already anchored near the eastern Pacific boundary, limiting further eastward displacement. However, examination of the temporal evolution of CESM2's MCA pattern (Figure 3a) reveals that while the coupling region cannot shift further east geographically, it becomes increasingly consolidated toward the eastern Pacific under warming. Despite this exception, models that exhibit greater thermocline shoaling generally show the largest eastward shifts of the air-sea coupling region, while those with thermocline deepening show a westward shift of the air-sea coupling center (Figures 4b,c), demonstrating that the coupling shift tracks the spatial pattern of thermocline depth change rather than simply responding to uniform warming. The depth of the thermocline determines where vertical advection is most effective at coupling subsurface temperature anomalies to the surface. As the thermocline shoals in the central Pacific west of 120°W, the region of maximum vertical coupling shifts with it, repositioning the Bjerknes feedback over a thermocline that is dynamically more responsive to wind-driven perturbations. Notably, in MPI models, the shoaling does not

extend westward of 180°, consistent with a more limited zonal shift in their coupling regions. The tight relationship between thermocline depth changes and shift in the air-sea coupling region identified here may also provide a clear physical pathway through which mean-state warming may enhance the oscillatory behavior of ENSO, as in Molina et al. (2026).

3.3 Forced Change in ENSO Event Frequency with Mean State

Under greenhouse warming scenarios, climate models project a more active ENSO regime, characterized by reduced time spent in neutral conditions and increased occurrence of both El Niño and La Niña states (Figure 5). The evolving trajectory of these changes, tracked via a 50-year sliding window (Figures 5a–c), reveals a progressive multi-decadal decline in neutral state frequency that accelerates after the 2000s across the majority of models (Figure 5b), accompanied by corresponding upward trajectories in both La Niña (Figure 5a) and El Niño (Figure 5c) occurrence. Comparing absolute event counts between the historical baseline (1950–1999) and the late 21st century (2050–2099) shows that, while historical simulations broadly capture observed frequency benchmarks from ERSSTv5 and HadISST, future radiative forcing redistributes phase occurrence (Figures 5d–f). Quantifying this forced response, neutral years decline in 7 of 10 models, with reductions ranging from 1 to 6 fewer neutral years per 50-year window (Figure 5h). Concurrently, the frequency of active ENSO phases increases across most models: La Niña frequency rises in 6 of 10 models, with forced increases ranging from 1 to 4.5 events per 50 years (Figure 5g), while El Niño frequency increases in 7 of 10 models, with changes of up to 2 additional events per 50 years (Figure 5i). Decomposing La Niña occurrence by duration reveals that this overall increase is predominantly driven by more frequent multi-year La Niña events—which increase significantly in 6 of 10 models, whereas single-year La Niña counts decrease or remain statistically unchanged in 8 of 10 models (Figure S6 in Supporting Information S1). The inter-member spread within each single-model large ensemble highlights the role of unforced internal variability, confirming that these shifts represent a forced emergent signal across the multi-model ensemble.

We also compare the change in DJF ENSO event frequency with the longitudinal shift of the MAM maximum air-sea coupling center across models (Figure 6). The correlation between longitude of maximum air-sea coupling and El Niño frequency is strong ($r = 0.67$), indicating that models with larger eastward shifts project greater increases

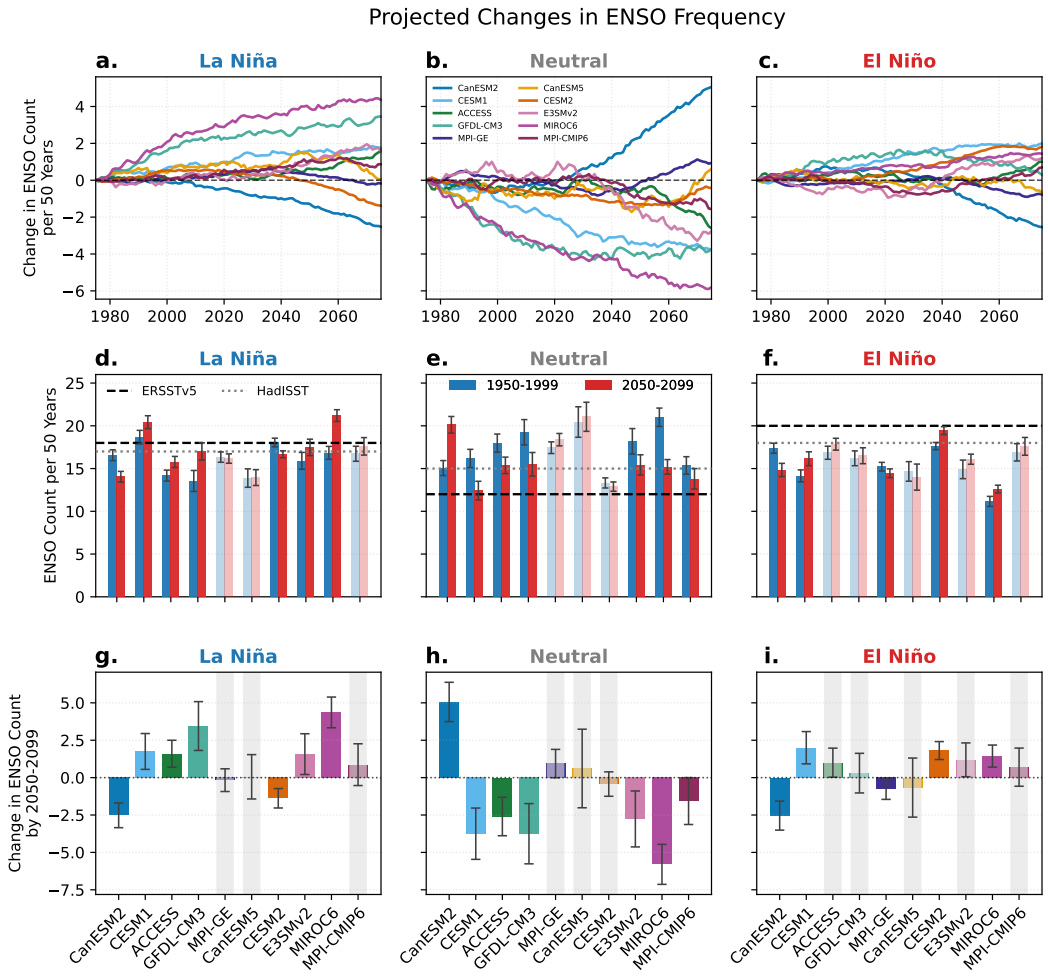

Figure 5. Projected Evolution of ENSO DJF Phase Frequency (1950-2100). Each column represents an ENSO phase: La Niña (left), Neutral (center), and El Niño (right). (a)–(c) Change in event count relative to the 1950–1999 baseline, computed using a 50-year sliding window. Each line shows the ensemble mean for a given model. (d)–(f) Event counts for each of the 10 selected models during the historical (1950–1999; blue bars) and late 21st century (2050–2099; red bars) periods. Horizontal black dashed and grey dotted lines indicate observed counts from ERSSTv5 and HadISST over 1950–1999, respectively. (g)–(i) Change in event frequency between the historical and future periods for each model. Error bars show the 95% confidence interval of the ensemble-mean change (two-tailed Student's t-test). Vertical grey shading in (d)–(i) marks models where the projected change is not statistically significant ($p > 0.05$; two-tailed Welch's t-test). All events are defined using the N3.4-m index.

in the number of El Niño events. A moderately negative correlation is found for neutral states ($r = -0.44$), suggesting some tendency for neutral frequency to decrease with eastward coupling shifts, though weaker than the El Niño relationship. No significant correlation emerges for La Niña ($r = 0.16$). This discrepancy suggests that eastward coupling shift primarily enhances the growth of El Niño events—likely by moving the Bjerknes feedback into a region of shallower thermocline where the feedback is more efficient at amplifying warm anomalies (Molina et al., 2026). Similar increases in El Niño frequency under greenhouse warming have been attributed to eastward shifts in the convective threshold and weakening of the zonal SST gradient (Cai et al., 2014, 2015). La Niña frequency, in contrast, may be governed by more complex processes, such as the residual effects of preceding heat discharge and the slow recharge of the equatorial heat reservoir, rather than simple zonal shifts in coupling (Okumura & Deser, 2010; Jia et al., 2025). While the sampling variability of the air-sea coupling region across members can be substantial, we find no clear association between the location and phase frequency without external forcing (Figure S7 in Supporting Information S1). This contrast suggests that the forced relationship identified across models likely does not arise from the coupling shift alone and would likely not be responsible for interdecadal variability of ENSO events in a static (non-warming) climate. Finally, we find no clear association between the strength of the air-sea coupling (SCF) and the frequency of occurrence of ENSO phases (Figure S8 in Supporting Information S1).

3.4 Forced Change in ENSO Phase Transitions with Mean State

Transitions between opposite ENSO phases become more frequent in the late twenty-first century, indicating a strengthening of ENSO's oscillatory behavior (Figure 7; see also Figure S9 in Supporting Information S1), consistent with Molina et al. (2026) and Freund et al. (2024). Across the 10 model large ensembles, six project an increase in the probability of La Niña-to-El Niño event transitions, whereby five are statistically significant (Figures 7a,d). Six models also project an increase in the probability of El Niño-to-La Niña event transitions, although only three are significant (Figures 7g,j). The more robust increase in La Niña-to-El Niño transitions in the future is particularly notable because this pathway occurs less frequently in instrumental observations. Under present-day conditions, La Niña events are more likely to persist or return to neutral than to transition directly into El Niño (Okumura & Deser, 2010; DiNezio & Deser, 2014), with in-

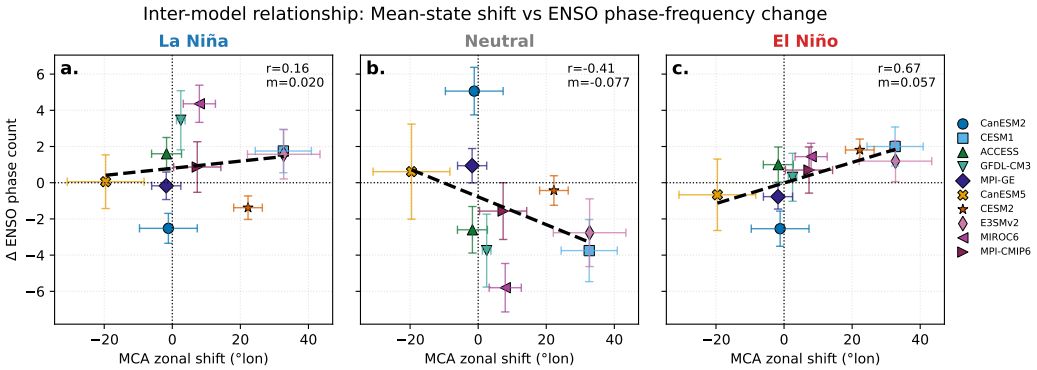

Figure 6. (a)–(c) Scatter plot of the projected shift in the longitude of maximum air-sea coupling in MAM (x-axis) and the change in DJF ENSO phase counts based on the N3.4-m index (y-axis) between 1950-1999 and 2050-2099 for (a) La Niña, (b) Neutral, and (c) El Niño states. Individual markers represent the ensemble mean for each of the 10 climate models, as identified in the legend. Horizontal and vertical error bars represent the 95% confidence interval of the ensemble-mean change (two-tailed Student's t-test) for the zonal shift and phase count changes, respectively. The dashed black line in each panel represents the inter-model linear regression, with the Pearson correlation coefficient (r) and slope (m) indicated in the upper-left corner.

dividual model trajectories revealing progressive multi-decadal departures from historical baselines across the 21st century (Figure S10 in Supporting Information S1).

We further stratify the La Niña to El Niño event transitions by differentiating between single-year La Niña events (Figures 7b,e,h,k) and multiyear La Niña events (Figures 7c,f,i,l). The probability of opposite phase transitions is heightened when considering multiyear La Niña events relative to single year La Niña events. This difference likely reflects the accumulated heat recharge that occurs during prolonged La Niña events: multiyear La Niña events reaccumulate more equatorial heat content than single-year events, preconditioning the system for a stronger subsequent El Niño (DiNezio et al., 2017; Jia et al., 2025). However, in the present-day climate, this accumulated recharge is often insufficient to trigger El Niño because the thermocline feedback in the central Pacific is too weak to amplify residual warm anomalies into a full El Niño event (Molina et al., 2026). Under greenhouse warming, the eastward shift of the coupling region into a zone of shallower thermocline may overcome this limitation, enabling the system to more efficiently convert accumulated heat into El Niño onset.

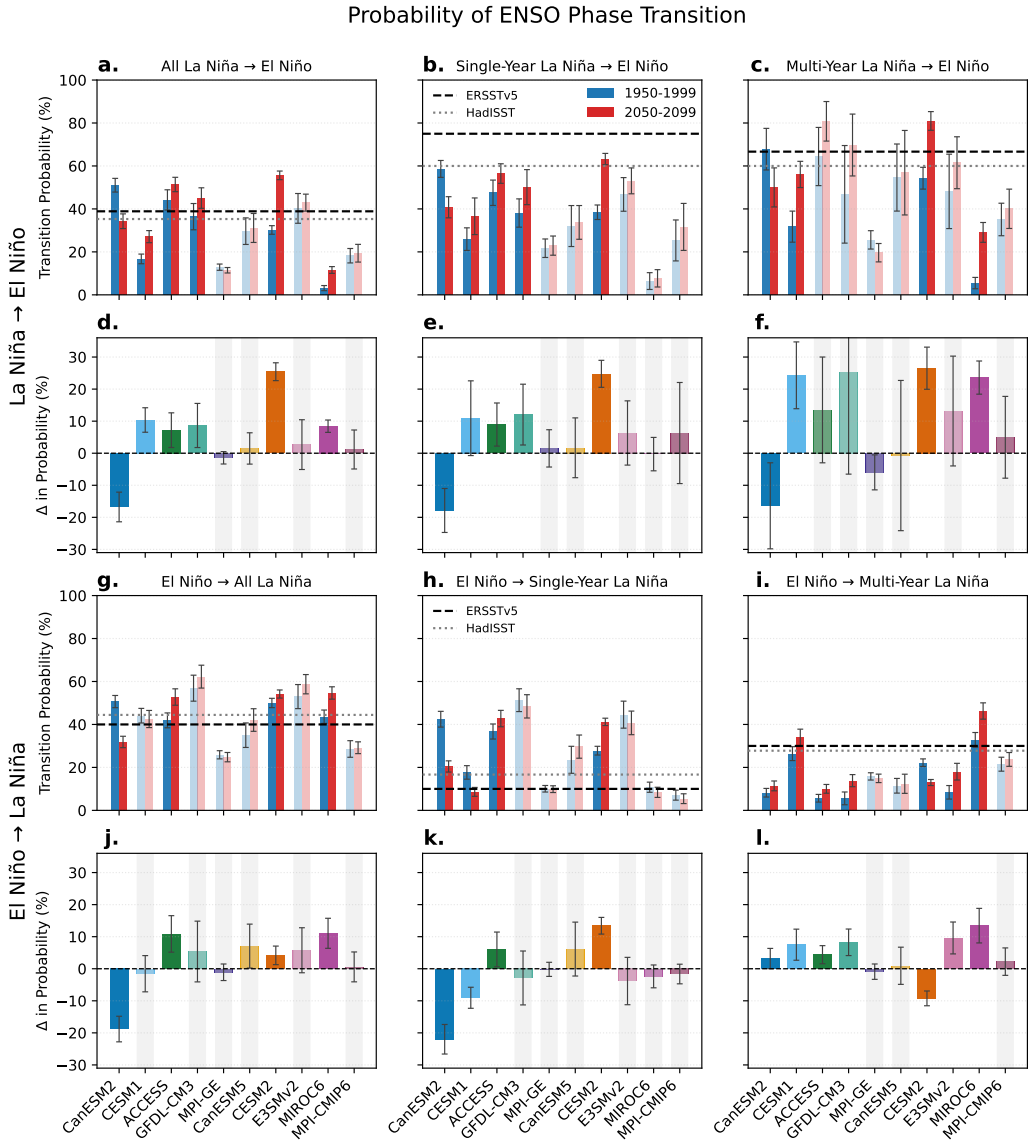

Figure 7. Projected changes in transitions between opposite ENSO phases, stratified by La Niña event duration. Phase transitions are organized by La Niña event duration category across columns: "All La Niña" (left), "Single-Year" (middle), and "Multi-Year" (right). (a)–(f) Transitions from La Niña to El Niño. (g)–(l) Transitions from El Niño to La Niña. (a)–(c) and (g)–(i) show transition probabilities for the historical (1950–1999; blue) and projected future (2050–2099; red) periods, with observational benchmarks from ERSSTv5 (black dashed line) and HadISST (grey dotted line). (d)–(f) and (j)–(l) show the projected shift (ΔP) in transition probabilities. Error bars represent the 95% confidence interval of the ensemble-mean change (two-tailed Student's t-test). Vertical grey shading in (d)–(f) and (j)–(l) marks models where the projected change is not statistically significant ($p > 0.05$; two-tailed Welch's t-test).

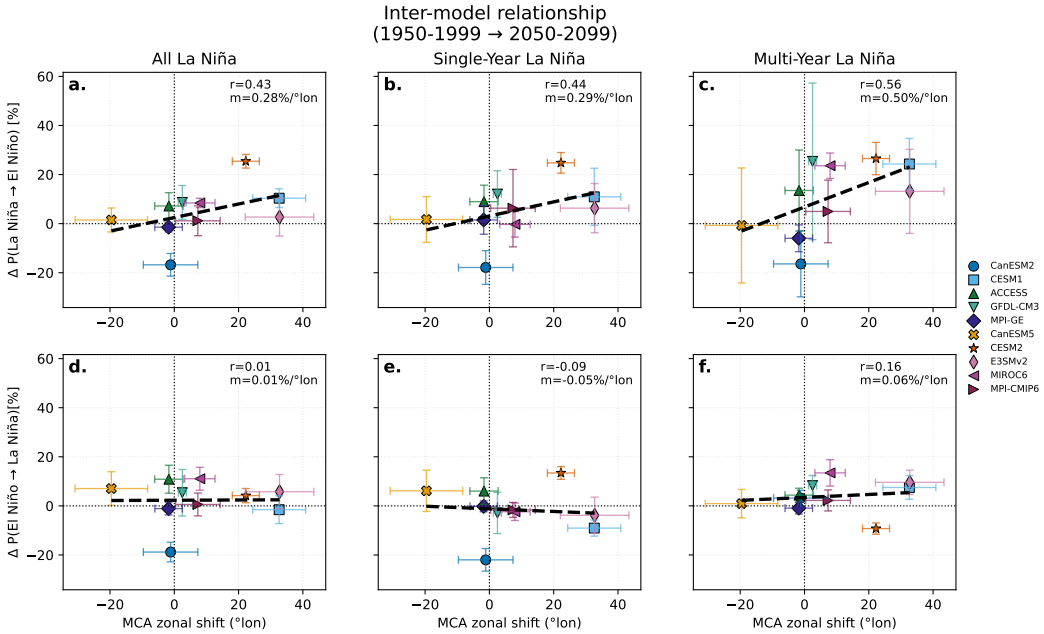

Figure 8. Inter-model relationship between zonal coupling shifts and ENSO transition probabilities. Columns represent La Niña duration categories: "All La Niña" (left), "Single-Year" (center), and "Multi-Year" (right), consistent with Figure 7. The x-axis shows the zonal shift in the center of action (Δlon; derived from the MCA patterns in Figure 3), where positive values indicate an eastward shift toward the eastern Pacific. The y-axis shows the change in transition probability (ΔP) between the historical (1950–1999) and projected future (2050–2099) periods. (a)–(c) La Niña-to-El Niño transitions for each duration category. (d)–(f) El Niño-to-La Niña transitions for each duration category. Each symbol represents the ensemble mean for a given model, with horizontal and vertical error bars showing the 95% confidence interval (two-tailed Student's t-test). Dashed black lines show the linear regression across models, with Pearson correlation coefficients (r) and slopes (m) displayed in each panel.

Across the MMLEAv2 archive, we find a robust, positive inter-model correlation between the magnitude of the forced eastward zonal shift and the increase in transition probability from La Niña-to-El Niño regardless of La Niña event duration (Figures 8a–c). While the correlation for all La Niña events is statistically significant ($r = 0.43$), the relationship strengthens considerably for multi-year La Niña events ($r = 0.56$; Figure 8c) compared to single-year La Niña events ($r = 0.44$; Figure 8b). In stark contrast, El Niño-to-La Niña transitions show no significant relationship to the longitude of maximum air-sea coupling, regardless of event duration (Figures 8d–f). Once again, the considerable internal variability of the longitude of maximum air-sea coupling is not obviously associated with variations in ENSO phase transitions (Figure S11 in Supporting Information S1). This contrast suggests that the forced relationship identified across models likely does not arise from the coupling shift alone but may arise from its interaction with broader mean-state changes under warming. We further note that the forced change in air-sea coupling strength (SCF) bears no meaningful relationship with the probability of ENSO transitioning from La Niña to El Niño (Figure S12 in Supporting Information S1) but may have a small influence on the probability of El Niño to La Niña phase transitions. The clear contrast between the SCF and MCA zonal shift metrics reinforces the idea that the spatial displacement of the air-sea coupling maximum—rather than the magnitude of the air-sea coupling—acts as a primary driver modulating ENSO oscillatory behavior across the MMLEAv2.

4 Discussion and Conclusions

This study illustrates that the zonal position of the boreal spring air-sea coupling maximum is a robust structural influence on ENSO behavior under greenhouse warming in ten model large ensembles. In the majority of models examined [6 out of 10 models], the air-sea coupling maximum shifts eastward, consistent with the weakening of the equatorial zonal SST gradient and eastward propagation of atmospheric deep convection (Vecchi & Soden, 2007). Furthermore, this eastward shift in maximum air-sea coupling can strengthen thermocline feedbacks across a diversity of mean climate states (Molina et al., 2026). This coupling shift is mechanistically tied to changes in the tropical Pacific thermocline: among the 8 models with an available Z_{20} field, the magnitude of thermocline shoaling within the N3.4-m region is strongly correlated with the eastward displacement of the coupling maximum (Figure 4c), indicating that the coupling region tracks

the spatial pattern of thermocline depth change rather than responding to uniform warming. We also find that the eastward shift in air-sea coupling is directly linked to an increase in the frequency of El Niño events, whereby models exhibiting larger eastward shifts project larger increases in El Niño events. Additionally, the probability of La Niña-to-El Niño phase transitions increases with this eastward shift in half of the 10 models, particularly when considering multi-year La Niña events. Critically, the large ensemble framework enables detection of these signals by separating the forced response from sampling variability at each time step—a capability that is impossible with a simple multi-model mean of single realizations (Deser et al., 2020). These results suggest that internal variability can drive substantial fluctuations in the location of maximum coupling without producing consistent changes in ENSO statistics. In contrast, the strongest ENSO response emerges only when the shift is sustained and driven by the forced mean-state reorganization of the tropical Pacific, implying that long-term changes in coupling location are necessary to alter ENSO's oscillatory behavior.

The influence of the eastward shift of the air-sea coupling maximum on ENSO phase transitions is not uniform across phases, further reflecting the asymmetry of ENSO (Figure 8). In the modern climate, El Niño-to-La Niña transitions are already efficient: El Niño events reliably discharge equatorial heat content and induce thermocline shoaling that rapidly cools the surface (Okumura & Deser, 2010). This pathway therefore depends less strongly on the longitude of maximum coupling. This discharge mechanism operates effectively regardless of where the coupling is centered because the strong El Niño wind response generates upwelling anomalies across a broad zonal extent. In contrast, La Niña-to-El Niño transitions are constrained by weak thermocline feedbacks in the central Pacific, where the deeper climatological thermocline limits the surface expression of subsurface warming anomalies (DiNezio & Deser, 2014; Molina et al., 2026). As the thermocline shoals west of 120°W under greenhouse warming, the region of maximum vertical coupling migrates with it, repositioning the Bjerknes feedback over a thermocline that is dynamically more responsive to wind-driven perturbations. An eastward shift of the maximum coupling region therefore places this feedback over a shallower thermocline, where subsurface anomalies more effectively influence SST and are more readily amplified into an El Niño. Molina et al. (2026) demonstrated this mechanism operates in equilibrium simulations of glacial to greenhouse conditions whereby an eastward shift of the air-sea coupling maximum strengthens the thermocline feedback and enhances ENSO's

oscillatory behavior. Our results show that this mechanism operates across multiple models under transient forcing: models with a larger eastward displacement of the air-sea coupling region project a more oscillatory ENSO cycle, characterized by more frequent and efficient phase transitions.

A particularly surprising result is that the eastward shift of the air-sea coupling region has a more pronounced influence on multi-year La Niña transitions to El Niño than on single-year La Niña transitions (Figures 8b,c). Multi-year La Niña events may become more frequent under greenhouse warming (Geng et al., 2023), though this projection is not robust across all studies (Chung et al., 2024) or across all models in our archive, for example CESM2 projects a significant decline of Multi-year La Niña in favor of single-year events (Figure S6 in Supporting Information S1). In either case, in the modern climate they rarely transition to El Niño (Okumura & Deser, 2010), a constraint that our results suggest will weaken as the coupling region shifts eastward. The enhanced sensitivity of multi-year transitions to coupling location likely reflects the accumulated heat recharge during prolonged cold events: multi-year La Niña events store more equatorial heat content than single-year events, providing a larger reservoir of warm anomalies that can be amplified if the thermocline feedback is sufficiently strong (DiNezio et al., 2017; Jia et al., 2025). Under greenhouse warming, the eastward positioning of the coupling center facilitates a more sensitive Bjerknes response during the late stages of an extended cold phase. Molina et al. (2026) linked this behavior to the shallow climatological thermocline of the eastern Pacific, where subsurface anomalies more efficiently influence SST. Jia et al. (2025) independently attributed this enhanced sensitivity to intensified upper-ocean stratification under warming, which strengthens ocean-atmosphere coupling and enables the system to more readily shift to El Niño. Both mechanisms—the shallow thermocline feedback and the enhanced stratification—enable the system to amplify residual warm anomalies more effectively, pulling the tropical Pacific out of prolonged La Niña states. Because multi-year La Niña-to-El Niño transitions are exceedingly rare in the modern climate, even a moderate increase in these transitions under warming represents a substantial fractional change. In contrast, no significant relationship is found between coupling longitude and changes in El Niño-to-La Niña transitions ($r = 0.01$; Figure 8d), reinforcing the conclusion that the eastward shift specifically targets the historically constrained La Niña-to-El Niño pathway rather than the already efficient discharge processes that trigger cold events.

Several caveats warrant consideration. The CMIP models exhibit well-known biases in tropical Pacific mean-state structure, including an equatorial cold tongue that is too pronounced and extends too far west (Bayr et al., 2018), which may affect the historical location of the coupling center and influence the magnitude of projected shifts. Additionally, two of the ten models are forced with SSP3-7.0 rather than RCP8.5 or SSP5-8.5; however, all scenarios share high greenhouse gas forcing, differing primarily in the evolution of aerosol forcing, which may modify the timing but not the direction of the forced response. We find the two SSP3-7.0 simulations fall within the range of the other eight models across all metrics considered. The transient nature of the simulations includes time-varying aerosol and ozone forcing that may modify the CO2 response, and recent observations suggest a strengthening Walker circulation that is at odds with model projections (Wills et al., 2022). Despite these uncertainties, the high-emission scenarios used here are appropriate for investigating how ENSO's oscillatory behavior evolves under substantial warming, and the consistency of the coupling-shift mechanism across models with different structural biases strengthens the robustness of the findings.

The relationship identified here between the boreal spring air-sea coupling region and ENSO transition behavior provides a strong foundation for future work. Targeted experiments that isolate zonal shifts in coupling from other mean-state changes would help clarify how coupling location, thermocline feedback efficiency, and upper-ocean stratification interact to shape ENSO evolution. In particular, an eastward shift in the coupling center may reorganize the dominant ENSO growth mechanism itself, favoring thermocline-driven eastern Pacific (EP-type) dynamics over zonal-advection-driven central Pacific (CP-type) behavior (Capotondi et al., 2015), and thus shifting ENSO flavor under warming. This framework could also be extended to changes in the likelihood of extreme eastern Pacific El Niño events through stronger thermocline feedbacks (Cai et al., 2018), and to evolving teleconnections associated with changes in the spatial pattern of tropical Pacific SST forcing and the resulting Rossby wave response (Timmermann et al., 2018). More broadly, our results suggest that future ENSO research may benefit from treating the coupling region not as a fixed background feature, but as a dynamically evolving component of the mean state.

Despite these uncertainties, the majority of models indicate that an eastward shift of the air-sea coupling center is a credible feature of ENSO change under high-emission scenarios. This result has direct implications for operational prediction systems, which

may need to recalibrate their statistical forecasts based on historical precursor relationships as the background state of the tropical Pacific changes. The projected intensification of ENSO's oscillatory component—particularly the enhanced La Niña-to-El Niño transition—has important implications for the duration, termination, and global impacts of La Niña events in a warming climate. A more active ENSO cycle with less time in neutral states increases the frequency of weather whiplash in teleconnected regions, affecting ecosystems and societies vulnerable to rapid shifts between drought and flood conditions (Okumura et al., 2017; Swain et al., 2025). At the same time, the large spread across ensemble members underscores that these projected changes will emerge against substantial internal variability, so individual decades may still depart markedly from the forced trend.

Conflict of Interest

The authors declare there are no conflicts of interest for this manuscript.

Data Availability Statement

The data presented in this study are publicly available. ERSSTv5 sea surface temperature data are available from the NOAA National Centers for Environmental Information at `https://www.ncei.noaa.gov/products/extended-reconstructed-sst` (Huang et al., 2017). HadISST data are available from the Met Office Hadley Centre at `https://www.metoffice.gov.uk/hadobs/hadisst/` (Rayner et al., 2003). ORAS5 ocean reanalysis data are available from the Copernicus Climate Change Service Climate Data Store at `https://doi.org/10.24381/cds.67e8eeb7` (Copernicus Climate Change Service, 2021). Large ensemble model output is available from the Multi-Model Large Ensemble Archive version 2 (MMLEAv2) at `https://www.cesm.ucar.edu/community-projects/mmlea/v2` (Maher et al., 2025).

Acknowledgments

BM was supported by the U.S. National Aeronautics and Space Administration (NASA) Oceanography Program Grant 80NSSC23K0358. SCS was supported by the U.S. National Aeronautics and Space Administration (NASA) Oceanography Program Grant 80NSSC23K0358, and the U.S. National Science Foundation (NSF) Grant OCE2303565. NM was supported by Australian Research Council grant no. DE230100315.

References

Bayr, T., Latif, M., Dommenget, D., Wengel, C., Harlaß, J., & Park, W. (2018). Mean-state dependence of ENSO atmospheric feedbacks in climate models. *Climate Dynamics*, *50*(9–10), 3171–3194. doi: 10.1007/s00382-017-3799-2

Bjerknes, J. (1969). Atmospheric teleconnections from the equatorial Pacific. *Monthly Weather Review*, *97*, 163–172. doi: 10.1175/1520-0493(1969)097⟨0163:ATFTEP⟩2.3.CO;2

Bretherton, C. S., Smith, C., & Wallace, J. M. (1992). An Intercomparison of Methods for Finding Coupled Patterns in Climate Data. *Journal of Climate*, *5*, 541–560. doi: 10.1175/1520-0442(1992)005⟨0541:AIOMFF⟩2.0.CO;2

Cai, W., Borlace, S., Lengaigne, M., van Rensch, P., Collins, M., Vecchi, G., ... Jin, F.-F. (2014). Increasing frequency of extreme El Niño events due to greenhouse warming. *Nature Climate Change*, *4*, 111–116. doi: 10.1038/nclimate2100

Cai, W., Wang, G., Dewitte, B., Wu, L., Santoso, A., Takahashi, K., ... McPhaden, M. J. (2015). Increased frequency of extreme La Niña events under greenhouse warming. *Nature Climate Change*, *5*, 132–137. doi: 10.1038/nclimate2492

Cai, W., Wang, G., Santoso, A., McPhaden, M. J., Wu, L., Jin, F.-F., ... Guilyardi, E. (2018). Increased variability of eastern Pacific El Niño under greenhouse warming. *Nature*, *564*, 201–206. doi: 10.1038/s41586-018-0776-9

Capotondi, A., Wittenberg, A. T., Newman, M., Di Lorenzo, E., Yu, J.-Y., Braconnot, P., ... Yeh, S.-W. (2015). Understanding ENSO diversity. *Bulletin of the American Meteorological Society*, *96*, 921–938. doi: 10.1175/BAMS-D-13-00117.1

Chung, C. T. Y., Power, S. B., Boschat, G., Gillett, Z. E., & Narsey, S. (2024). Projected Changes to Characteristics of El Niño–Southern Oscillation, Indian Ocean Dipole, and Southern Annular Mode Events in the CMIP6 Models. *Earth's Future*, *12*(11). doi: 10.1029/2024EF005166

Conti, G., Navarra, A., & Tribbia, J. (2017). The ENSO Transition Probabilities. *Journal of Climate*, *30*, 4951–4964. doi: 10.1175/JCLI-D-16-0490.1

Copernicus Climate Change Service. (2021). *ORAS5 global ocean reanalysis monthly data from 1958 to present.* Copernicus Climate Change Service Climate Data Store. Retrieved from `https://doi.org/10.24381/cds.67e8eeb7` doi: 10

.24381/cds.67e8eeb7

Deser, C., Lehner, F., Rodgers, K. B., Aarons, T., Delworth, C., DiNezio, P. N., ... Ting, M. (2020). Insights from Earth system model initial-condition large ensembles and future prospects. *Nature Climate Change*, *10*, 277–286. doi: 10.1038/s41558-020-0731-2

Deser, C., Phillips, A. S., Tomas, R. A., Okumura, Y. M., Alexander, M. A., Capotondi, A., ... Ohba, M. (2012). ENSO and Pacific decadal variability in the Community Climate System Model version 4. *Journal of Climate*, *25*, 2622–2651. doi: 10.1175/JCLI-D-11-00301.1

DiNezio, P. N., & Deser, C. (2014). Nonlinear controls on the persistence of La Niña. *Journal of Climate*, *27*, 7335–7355. doi: 10.1175/JCLI-D-14-00033.1

DiNezio, P. N., Deser, C., Karspeck, A., Yeager, S., Okumura, Y., Danabasoglu, G., ... Meehl, G. A. (2017). A 2 year forecast for a 60–80% chance of La Niña in 2017–2018. *Geophysical Research Letters*, *44*, 11624–11635. doi: 10.1002/2017GL074904

Fasullo, J. T., Golaz, J.-C., Caron, J. M., Rosenbloom, N., Meehl, G. A., Strand, W., ... Bartoletti, T. (2024). An overview of the E3SM version 2 large ensemble and comparison to other E3SM and CESM large ensembles. *Earth System Dynamics*, *15*, 367–386. doi: 10.5194/esd-15-367-2024

Fedorov, A. V., & Philander, S. G. (2001). A stability analysis of tropical ocean–atmosphere interactions: Bridging measurements and theory for El Niño. *Journal of Climate*, *14*(14), 3086–3101. doi: 10.1175/1520-0442(2001)014⟨3086:ASAOTO⟩2.0.CO;2

Freund, M. B., Brown, J. R., Marshall, A. G., Tozer, C. R., Henley, B. J., Risbey, J. S., ... Sharmila, S. (2024). Interannual ENSO diversity, transitions, and projected changes in observations and climate models. *Environmental Research Letters*, *19*, 114005. doi: 10.1088/1748-9326/ad78db

Geng, T., Cai, W., Wu, L., & Yang, Y. (2019). Atmospheric convection dominates genesis of ENSO asymmetry. *Geophysical Research Letters*, *46*(14), 8387–8396. doi: 10.1029/2019GL083802

Geng, T., Jia, F., Cai, W., Wu, L., Gan, B., Jing, Z., ... McPhaden, M. J. (2023). Increased occurrences of consecutive La Niña events under global warming. *Nature*, *619*, 774–781. doi: 10.1038/s41586-023-06236-9

Graham, N. E., & Barnett, T. P. (1987). Sea Surface Temperature, Surface Wind Divergence, and Convection over Tropical Oceans. *Science*, *238*(4827), 657–659. doi: 10.1126/science.238.4827.657

Huang, B., Thorne, P. W., Banzon, V. F., Boyer, T., Chepurin, G., Lawrimore, J. H., ... Zhang, H.-M. (2017). Extended Reconstructed Sea Surface Temperature, version 5 (ERSSTv5): Upgrades, validations, and intercomparisons. *Journal of Climate*, *30*, 8179–8205. doi: 10.1175/JCLI-D-16-0836.1

Jia, F., Cai, W., Geng, T., Gan, B., Zhong, W., Wu, L., & McPhaden, M. J. (2025). Transition from multi-year La Niña to strong El Niño rare but increased under global warming. *Science Bulletin*, *70*, 756–764. doi: 10.1016/j.scib.2024.12.034

Jin, F.-F. (1997). An equatorial ocean recharge paradigm for ENSO. Part I: Conceptual model. *Journal of the Atmospheric Sciences*, *54*, 811–829. doi: 10.1175/1520-0469(1997)054⟨0811:AEORPF⟩2.0.CO;2

Kang, I.-S., & Kug, J.-S. (2002). El Niño and La Niña sea surface temperature anomalies: Asymmetry characteristics associated with their wind stress anomalies. *Journal of Geophysical Research*, *107*(D19). doi: 10.1029/2001JD000393

Kay, J. E., Deser, C., Phillips, A., Mai, A., Hannay, C., Strand, G., ... Vertenstein, M. (2015). The Community Earth System Model (CESM) large ensemble project: A community resource for studying climate change in the presence of internal climate variability. *Bulletin of the American Meteorological Society*, *96*, 1333–1349. doi: 10.1175/BAMS-D-13-00255.1

Kessler, W. S. (1990). Observations of long Rossby waves in the northern tropical Pacific. *JGR*, *95*(C4), 5183–5217. doi: 10.1029/JC095iC04p05183

Kessler, W. S. (2002). Is ENSO a cycle or a series of events? *Geophysical Research Letters*, *29*, 2125. doi: 10.1029/2002GL015924

Kirchmeier-Young, M., Zwiers, F., & Gillett, N. (2017). Attribution of Extreme Events in Arctic Sea Ice Extent. *Journal of Climate*, *30*, 5535–5571. doi: 10.1175/JCLI-D-16-0412.1

Li, G., Du, Y., Xu, H., & Ren, B. (2015). An intermodel approach to identify the source of excessive equatorial Pacific cold tongue in CMIP5 models and uncertainty in observational datasets. *Journal of Climate*, *28*(19), 7630–7640. doi: 10.1175/JCLI-D-15-0166.1

Li, G., & Xie, S.-P. (2014). Tropical biases in CMIP5 multimodel ensemble: The excessive equatorial Pacific cold tongue and double ITCZ problems. *Journal of Climate*, *27*(4), 1765–1780. doi: 10.1175/JCLI-D-13-00337.1

Li, G., Xie, S.-P., Du, Y., & Luo, Y. (2016). Effects of excessive equatorial cold tongue bias on the projections of tropical Pacific climate change. Part I: The warming pattern in CMIP5 multi-model ensemble. *Climate Dynamics*, *47*(12), 3817–3831. doi: 10.1007/s00382-016-3043-5

Maher, N., Milinski, S., Suarez-Gutierrez, L., Botzet, M., Dobrynin, M., Kornblueh, L., ... Marotzke, J. (2019). The Max Planck Institute Grand Ensemble: Enabling the Exploration of Climate System Variability. *Journal of Advances in Modeling Earth Systems*, *11*, 2050–2069. doi: 10.1029/2019MS001639

Maher, N., Phillips, A. S., Deser, C., Wills, R. C. J., Lehner, F., Fasullo, J., ... Jeffree, J. (2025). The updated Multi-Model Large Ensemble Archive and the Climate Variability Diagnostics Package: new tools for the study of climate variability and change. *Geoscientific Model Development*, *18*, 6341–6365. doi: 10.5194/gmd-18-6341-2025

Maher, N., Wills, R. C. J., DiNezio, P., Klavans, J., Milinski, S., Sanchez, S. C., ... Wu, X. (2023). The future of the El Niño–Southern Oscillation: Using large ensembles to illuminate time-varying responses and inter-model differences. *Earth System Dynamics*, *14*, 413–431. doi: 10.5194/esd-14-413-2023

McPhaden, M. J., Zebiak, S. E., & Glantz, M. H. (2006). ENSO as an integrating concept in Earth science. *Science*, *314*, 1740–1745. doi: 10.1126/science.1132588

Meinen, C. S., & McPhaden, M. J. (2000). Observations of Warm Water Volume Changes in the Equatorial Pacific and Their Relationship to El Niño and La Niña. *Journal of Climate*, *13*, 3551–3559. doi: 10.1175/1520-0442(2000)013⟨3551:OOWWVC⟩2.0.CO;2

Molina, B. A., DiNezio, P. N., & Deser, C. (2026). Changes in ENSO Oscillatory Dynamics Associated with Zonal Shifts in Air–Sea Coupling Region. *Journal of Climate*, *39*, 3631–3652. doi: 10.1175/JCLI-D-25-0074.1

Okumura, Y. M., & Deser, C. (2010). Asymmetry in the duration of El Niño and La Niña. *Journal of Climate*, *23*, 5826–5843. doi: 10.1175/2010JCLI3592.1

Okumura, Y. M., DiNezio, P., & Deser, C. (2017). Evolving Impacts of Multiyear La

Niña Events on Atmospheric Circulation and U.S. Drought. *Geophysical Research Letters*, *44*. doi: 10.1002/2017GL075034

Olonscheck, D., Suarez-Gutierrez, L., Milinski, S., Beobide-Arsuaga, G., Baehr, J., Fröb, F., ... Brune, S. (2023). The New Max Planck Institute Grand Ensemble With CMIP6 Forcing and High-Frequency Model Output. *Journal of Advances in Modeling Earth Systems*, *15*, e2023MS003790. doi: 10.1029/2023MS003790

Rayner, N. A., Parker, D. E., Horton, E. B., Folland, C. K., Alexander, L. V., Rowell, D. P., ... Kaplan, A. (2003). Global analyses of sea surface temperature, sea ice, and night marine air temperature since the late nineteenth century. *Journal of Geophysical Research*, *108*. doi: 10.1029/2002JD002670

Rodgers, K. B., Lee, S.-S., Rosenbloom, N., Timmermann, A., Danabasoglu, G., Deser, C., ... Yeager, S. G. (2021). Ubiquity of human-induced changes in climate variability. *Earth System Dynamics*, *12*, 1393–1411. doi: 10.5194/esd-12-1393-2021

Stuecker, M. F., Timmermann, A., Jin, F.-F., McGregor, S., & Ren, H.-L. (2013). A combination mode of the annual cycle and the El Niño/Southern Oscillation. *Nature Geoscience*, *6*, 540–544. doi: 10.1038/ngeo1826

Sun, L., Alexander, M., & Deser, C. (2018). Evolution of the Global Coupled Climate Response to Arctic Sea Ice Loss during 1990–2090 and Its Contribution to Climate Change. *Journal of Climate*, *31*, 7823–7843. doi: 10.1175/JCLI-D-18-0134.1

Swain, D. L., Prein, A. F., Abatzoglou, J. T., Albano, C. M., Brunner, M., Diffenbaugh, N. S., ... Touma, D. (2025). Hydroclimate volatility on a warming Earth. *Nature Reviews Earth & Environment*, *6*, 35–50. doi: 10.1038/s43017-024-00624-z

Swart, N. C., Cole, J. N. S., Kharin, V. V., Lazare, M., Scinocca, J. F., Gillett, N. P., ... Winter, B. (2019). The Canadian Earth System Model version 5 (CanESM5.0.3). *Geoscientific Model Development*, *12*, 4823–4873. doi: 10.5194/gmd-12-4823-2019

Takahashi, K., & Dewitte, B. (2016). Strong and moderate nonlinear El Niño regimes. *Climate Dynamics*, *46*, 1627–1645. doi: 10.1007/s00382-015-2665-3

Tatebe, H., Ogura, T., Nitta, T., Komuro, Y., Ogochi, K., Takemura, T., ... Ki-

moto, M. (2019). Description and basic evaluation of simulated mean state, internal variability, and climate sensitivity in MIROC6. *Geoscientific Model Development*, *12*, 2727–2765. doi: 10.5194/gmd-12-2727-2019

Timmermann, A., An, S.-I., Kug, J.-S., Jin, F.-F., Cai, W., Capotondi, A., ... Zhang, X. (2018). El Niño–Southern Oscillation complexity. *Nature*, *559*, 535–545. doi: 10.1038/s41586-018-0252-6

Torrence, C., & Webster, P. J. (1998). The annual cycle of persistence in the El Niño/Southern Oscillation. *Quarterly Journal of the Royal Meteorological Society*, *124*(550), 1985–2004. doi: 10.1002/qj.49712455010

Trenberth, K. E. (1997). The definition of El Niño. *Bulletin of the American Meteorological Society*, *78*, 2771–2777. doi: 10.1175/1520-0477(1997)078⟨2771:TDOENO⟩2.0.CO;2

Vecchi, G. A., & Soden, B. J. (2007). Global warming and the weakening of the tropical circulation. *Journal of Climate*, *20*, 4316–4340. doi: 10.1175/JCLI4258.1

Webster, P. J., & Yang, S. (1992). Monsoon and ENSO: Selectively Interactive Systems. *Quarterly Journal of the Royal Meteorological Society*, *118*, 877–926. doi: 10.1002/qj.49711850705

Wills, R. C. J., Dong, Y., Proistosecu, C., Armour, K. C., & Battisti, D. S. (2022). Systematic Climate Model Biases in the Large-Scale Patterns of Recent Sea-Surface Temperature and Sea-Level Pressure Change. *Geophysical Research Letters*, *49*(17). doi: 10.1029/2022GL100011

Wittenberg, A. T. (2009). Are historical records sufficient to constrain ENSO simulations? *Geophysical Research Letters*, *36*, L12702. doi: 10.1029/2009GL038710

Yang, H., & Wang, F. (2009). Revisiting the thermocline depth in the equatorial Pacific. *Journal of Climate*, *22*(13), 3856–3863. doi: 10.1175/2009JCLI2829.1

Ziehn, T., Chamberlain, M. A., Law, R. M., Lenton, A., Bodman, R. W., Dix, M., ... Srbinovsky, J. (2020). The Australian Earth System Model: ACCESS-ESM1.5. *Journal of Southern Hemisphere Earth System Science*, *70*, 193–214. doi: 10.1071/ES19035

Zuo, H., Balmaseda, M. A., Tietsche, S., Mogensen, K., & Mayer, M. (2019). The ECMWF operational ensemble reanalysis–analysis system for ocean and sea

ice: A description of the system and assessment. *Ocean Science*, *15*, 779–808.
doi: 10.5194/os-15-779-2019